Ocean Surface Boundary Layer Response to Abruptly Turning Winds

XINGCHI WANG[a] AND TOBIAS KUKULKA[a]

[a] *University of Delaware, Newark, Delaware*

ABSTRACT: Turbulence driven by wind and waves controls the transport of heat, momentum, and matter in the ocean surface boundary layer (OSBL). For realistic ocean conditions, winds and waves are often neither aligned nor constant, for example, when winds turn rapidly. Using a large-eddy simulation (LES) method, which captures shear-driven turbulence (ST) and Langmuir turbulence (LT) driven by the Craik–Leibovich vortex force, we investigate the OSBL response to abruptly turning winds. We design idealized LES experiments in which winds are initially constant to equilibrate OSBL turbulence before abruptly turning 90° either cyclonically or anticyclonically. The transient Stokes drift for LT is estimated from a spectral wave model. The OSBL response includes three successive stages that follow the change in direction. During stage 1, turbulent kinetic energy (TKE) decreases as a result of reduced TKE production. Stage 2 is characterized by TKE increasing, with TKE shear production recovering and exceeding TKE dissipation. Transient TKE levels may exceed their stationary values because of inertial resonance and nonequilibrium turbulence. Turbulence relaxes to its equilibrium state at stage 3, but LT still adjusts as a result of slowly developing waves. During stages 1 and 2, greatly misaligned wind and waves lead to Eulerian shear TKE production exceeding Stokes drift shear TKE production. A Reynolds stress budget analysis and Reynolds-averaged Navier–Stokes equation models indicate that Stokes drift shear production furthermore drives the OSBL response. The Coriolis effects result in asymmetrical OSBL responses to wind turning directions. Our results suggest that transient wind conditions play a key role in understanding realistic OSBL dynamics.

KEYWORDS: Turbulence; Wind waves; Atmosphere–ocean interaction; Langmuir circulation; Oceanic mixed layer; Large-eddy simulations

1. Introduction

The ocean surface boundary layer (OSBL) is essential for air–sea interaction processes because OSBL turbulence transports heat, salt, momentum, and suspended and dissolved matter. OSBL turbulence is driven by wind and waves (Thorpe 2004; Sullivan and McWilliams 2010; D'Asaro 2014). Many idealized process studies of the OSBL assume that the forcing wind and waves are constant and aligned. However, typical ocean conditions are often characterized by highly variable wind and wave conditions. The goal of this study is to investigate how the OSBL responds to suddenly changing wind directions.

This study focuses on wind and wave-driven turbulence. Nonbreaking waves influence OSBL turbulence through the interaction between the Stokes drift (residual circulation caused by greater below-crest and smaller bellow-trough wave orbital speeds) and Eulerian currents (Craik and Leibovich 1976). The Stokes drift tilts vertical vorticity into the wave propagation direction through the Craik–Leibovich (CL) vortex force (Craik and Leibovich 1976), resulting in counterrotating vortices that are approximately aligned with the wind, which are referred to as Langmuir circulation (LC; Langmuir 1938). LCs are characterized by a hierarchy of irregular spatial and temporal scales, and therefore also identified as Langmuir turbulence (LT; McWilliams et al. 1997). Recent studies indicate that LT plays an important role in OSBL dynamics, enhancing the vertical fluxes of momentum and heat, inducing stronger vertical velocity variance, and facilitating mixed

layer deepening (Thorpe 2004; Sullivan and McWilliams 2010; D'Asaro et al. 2014).

A common modeling tool of LT is a large-eddy simulation (LES) approach based on the filtered CL equations (Skyllingstad and Denbo 1995; McWilliams et al. 1997). LES results are consistent with the observed LT characteristics, such as strong surface convergence regions (Farmer and Li 1995; Thorpe 2004; Kukulka et al. 2009), and enhanced vertical velocity variance (Gargett et al. 2004; D'Asaro 2014). However, idealized LES process studies of the OSBL often assume constant wind forcing (e.g., McWilliams et al. 1997; Li et al. 2005; Harcourt and D'Asaro 2008; Van Roekel et al. 2012), although winds over the ocean are rarely constant.

Only a few previous LES studies of the OSBL investigate transient wind and wave forcing. The study of Skyllingstad et al. (2000) finds that resonantly rotating winds generate larger currents and stronger vertical mixing. Kukulka et al. (2013) indicate that the presence of swell generates larger mixing to inhibit upper-ocean restratification in low-wind conditions. Sullivan et al. (2012) and Wang et al. (2018) show that the LT evolution greatly depends on the transient state of wind and waves under tropical cyclones.

This study examines the OSBL response to rapidly turning winds, which are commonly observed over the ocean (Fig. 1). This is a challenging problem because the wave field slowly turns and adjusts to the new wind direction (top panels of Fig. 2; Holthuijsen et al. 1987; van Vledder and Holthuijsen 1993). In the next section, we introduce an idealized LES approach to model OSBL turbulence with transient wind and wave forcing. In the results section, we first identify nonequilibrium turbulence based on a bulk TKE analysis for cyclonically and anticyclonically turning winds with (LT) and

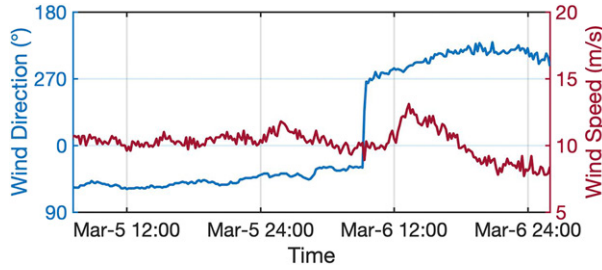*Corresponding author*: Xingchi Wang, wangxch@udel.edu

FIG. 1. Observed wind direction (blue line) and speed (red line) for an abruptly turning wind event in 2015 from NDBC buoy station 41002, located in the Atlantic Ocean about 420 km south of Cape Hatteras.

without (shear-driven turbulence, ST) wave effects (section 3a). We then explore in detail the OSBL response for the simplest case with cyclonically turning winds and ST (section 3b) before highlighting differences between ST and wave-driven LT (section 3c). The last part of the results (section 3d) contrasts the OSBL responses for cyclonically and anticyclonically turning winds before concluding with section 4.

2. OSBL turbulence models for abruptly turning winds

a. Basic experimental design

Four LES experiments are designed to study the OSBL responses to abruptly turning winds, two with surface wave forcing and two without. We first apply a constant northward (y direction) wind stress τ with an ocean friction velocity $u_* = 0.0133$ m s^{-1} to generate fully developed turbulence before the wind turns, where $u_* = (\tau/\rho_0)^{1/2}$ and $\rho_0 = 1024$ kg m^{-3} is a reference ocean density. This u_* corresponds to a wind speed at 10 m height of $U_{10} = 10$ m s^{-1}. For LT, we include the wave forcing driven by the same wind (see below). The initial

temperature is set constant with a depth of 33 m; below this depth, temperature decreases at a rate of 0.01°C m^{-1}. OSBL deepening and buoyancy entrainment at the OSBL base are weak for the experimental conditions. After the turbulence reaches a stationary state, we abruptly turn the wind direction by 90° either cyclonically (in the negative x direction; case C) or anticyclonically (in the positive x direction; case AC) for both ST and LT cases (Table 1).

b. LES model

The LES model of turbulent OSBL currents is based on the grid-filtered CL equations and is described by McWilliams et al. (1997). The governing momentum equation is

$$\frac{\partial \tilde{u}_i}{\partial t} + \tilde{u}_j \frac{\partial \tilde{u}_i}{\partial x_j} + \epsilon_{ikm} f_k (\tilde{u}_m + u_{s,m}) = -\frac{\partial \tilde{\pi}}{\partial x_i} + \frac{\tilde{\rho}}{\rho_0} g_i$$
$$+ \epsilon_{ikm} u_{s,k} \tilde{\omega}_m + \text{SGS}, \qquad (1)$$

where t denotes time; the Cartesian coordinates $(x_1, x_2, x_3) = (x, y, z)$ include components toward east, north, and upward, respectively; $(u_1, u_2, u_3) = (u, v, w)$ is the velocity vector; $(u_{s,1}, u_{s,2}, u_{s,3}) = (u_s, v_s, 0)$ is the Stokes drift vector; $(f_1, f_2, f_3) = (0, 0, f)$ is the Coriolis vector with the Coriolis parameter $f = 10^{-4}$ s^{-1}; $(g_1, g_2, g_3) = (0, 0, -g)$ is Earth's acceleration vector with $g = 9.81$ m s^{-2}; $\pi = (p/\rho_0) + 1/2[(u_i + u_{s,i})(u_i + u_{s,i}) - u_i u_i]$ is the generalized pressure in which p is the pressure; ρ is the water density; $\omega_i = \epsilon_{ikm}(\partial/\partial x_k)u_m$ is the relative vorticity; and ϵ_{ikm} is the permutation tensor. The LES method decomposes variables into resolved components, indicated by a tilde, and subgrid-scale components denoted by SGS (Moeng 1984). The CL vortex force $\epsilon_{ikm}u_{s,k}\omega_m$ is equal to the cross product of Stokes drift and vorticity vectors, describing the interaction between nonbreaking waves and Eulerian currents. The CL vortex force is zero for ST so that the LES model simply captures shear and buoyancy instabilities.
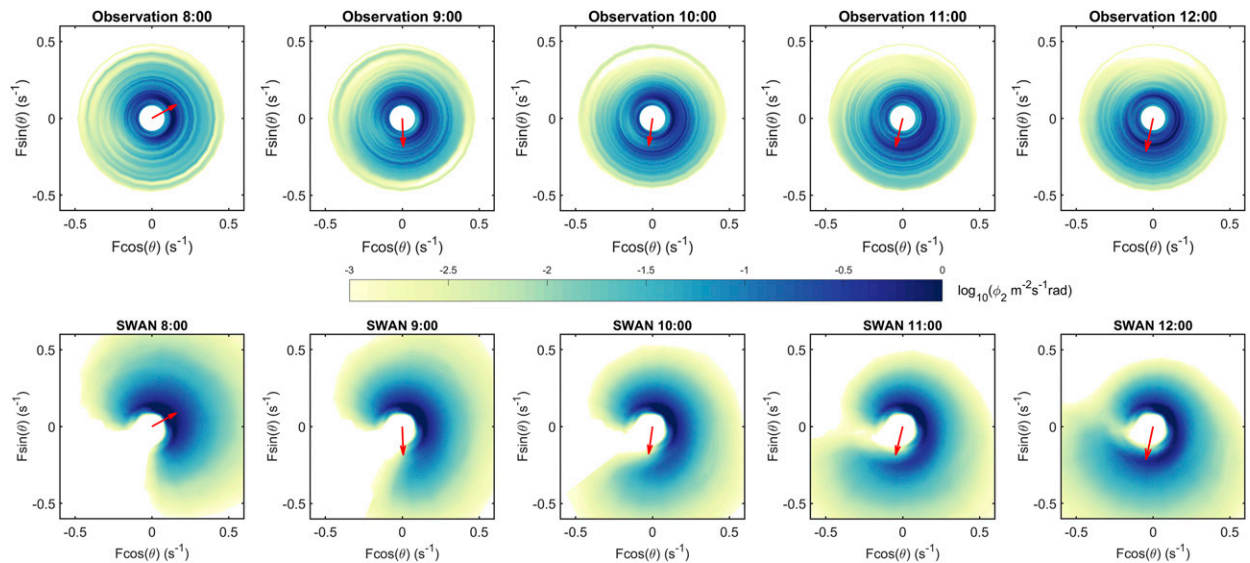

FIG. 2. (top) Observed and (bottom) simulated two-dimensional wave height spectrum $\phi_2(F, \theta)$, where F is the wave frequency, and θ is the wave propagation direction, coinciding with the abruptly turning wind event from Fig. 1. The red arrow represents the wind vector.

TABLE 1. Experiment settings for OSBL turbulence response under abruptly wind direction changing.

Cases	Wind changing direction	U_{10} (m s^{-1})	u_* (m s^{-1})	Wave input
C-ST	North → west	10	0.0133	No
AC-ST	North → east	10	0.0133	No
C-LT	North → west	10	0.0133	Yes
AC-LT	North → east	10	0.0133	Yes

The Stokes drift vector in Eq. (1) is obtained from the two-dimensional wave height spectrum ϕ_2 (Kenyon 1969):

$$\mathbf{u}_s(z) = \frac{16\pi^3}{g} \int_0^\infty \int_{-\pi}^{\pi} \hat{\mathbf{k}} F^3 \phi_2(F,\theta) e^{2kz} \, d\theta \, dF, \qquad (2)$$

where $\mathbf{k}$ is the wavenumber vector, $k = |\mathbf{k}|$ is the magnitude of wavenumber vector, and $\hat{\mathbf{k}} = \mathbf{k}/k$ is the unit vector in the direction of waves; $F = (gk)^{1/2}/(2\pi)$ is the wave frequency, which assumes the deep water dispersion relation; θ is the direction of wave propagation. To capture the transient wave response, ϕ_2 is simulated by a spectral wave model (described in section 2d).

The default LES modeling domain spans a 150 m × 150 m horizontal and 150-m-deep ocean volume with 128 × 128 horizontal grid points and 256 vertical grid points. The grid resolution is $\Delta x = \Delta y = 1.17$ m in the horizontal plane and $\Delta z = 0.59$ m in the vertical direction. Sensitivity experiments with 64 × 64 × 128 and 256 × 256 × 512 grid points indicate that the resolution of 128 × 128 × 256 successfully resolves the flux and energy carrying eddies for both ST and LT after the wind turns.

c. RANS model

We compare LES results with Reynolds-averaged Navier–Stokes (RANS) models that are commonly the basis for larger-scale ocean models. The RANS model is implemented for the four LES experiments (Table 1), which is (e.g., McWilliams et al. 1997),

$$\frac{\partial \langle u_i \rangle}{\partial t} + \epsilon_{ikm} f_k (\langle u_m \rangle + u_{s,m}) = -\frac{\partial \langle u_i' w' \rangle}{\partial z}, \qquad (3)$$

where angle brackets represent the horizontal average and variables with primes are deviations from horizontal averages. The vertical turbulent momentum flux $\langle u_i' w' \rangle$ needs to be parameterized in RANS models. Usually, an eddy viscosity ν_e is employed such that

$$\langle u_i' w' \rangle = -\nu_e \frac{\partial \langle u_i \rangle}{\partial z}. \qquad (4)$$

In this study, we apply the K-profile parameterization (KPP; Large et al. 1994) model and the second-moment closure (SMC; Kantha and Clayson 1994) model as the turbulent closure models to obtain ν_e. Furthermore, we consider two variants with and without explicit LT effects for each closure model.

Without explicit LT effects, the KPP model parameterizes the eddy viscosity from the boundary layer depth h_b, a turbulent velocity scale $w_\lambda(\sigma)$, and a dimensionless shape function $G_\lambda(\sigma)$ so that

$$\nu_e(\sigma) = h_b w_\lambda(\sigma) G_\lambda(\sigma), \qquad (5)$$

where the nondimensional depth is $\sigma = -z/h_b$. The boundary layer depth is diagnosed by a bulk Richardson number criterion (Large et al. 1994).

The SMC model closes the turbulence equations at second-moment level, and combines two nonequilibrium prognostic equations for TKE (TKE = $\langle u_i' u_i' \rangle / 2 = q^2/2$, where q is the turbulent velocity scale) and the product of turbulence length scale l and 2 times the TKE ($q^2 l$), called the level-2.5 SMC model (Kantha and Clayson 1994). The eddy viscosity based on SMC model is expressed as

$$\nu_e = S_M q l, \qquad (6)$$

where S_M is a stability function determined from a second-moment algebraic closure for an equilibrium state.

Recently, several studies proposed modifications of those turbulence closure models to explicitly include LT (McWilliams et al. 2012, 2014; Harcourt 2013, 2015; Reichl et al. 2016; Li et al. 2017; Reichl and Li 2019). We select the KPP-LT model modified by Reichl et al. (2016), which uses a Lagrangian velocity to compute the turbulent momentum flux and adds a turbulence enhancement factor originally proposed by McWilliams and Sullivan (2000),

$$\langle u_i' w' \rangle = -\nu_e^L \frac{\partial \langle u_i^L \rangle}{\partial z}, \qquad (7)$$

where u_i^L is the Lagrangian velocity, which is the sum of Eulerian and Stokes drift velocity, and ν_e^L is an eddy viscosity based on u_i^L.

The SMC model for LT (SMC-LT) proposed by Harcourt (2015), which considers the CL vortex force production terms, is also used in this study,

$$\langle u_i' w' \rangle = -S_M q l \frac{\partial \langle u_i \rangle}{\partial z} - S_M^S q l \frac{\partial u_{s,i}}{\partial z}, \qquad (8)$$

where S_M^S is a stability function related to Stokes drift shear contributions.

The different turbulent closure models are implemented using the General Ocean Turbulence Model (GOTM; Umlauf and Burchard 2005). Specifically, the version modified by Li et al. (2019), which includes KPP-LT and SMC-LT closure models, is used in this study. The initial density profile, wind and wave forcing, vertical resolution, and spin up time of the RANS model are the same as those of the LES model.

d. Wave model and test application

A robust estimate of the developing wave field is necessary for accurately modeling LT. The third-generation wave model Simulating Wave Nearshore (SWAN; Booij et al. 1997) is

applied to obtain the directional frequency spectra of surface gravity waves under suddenly turning winds. This study mainly focuses on wind-driven gravity waves in deep water, thus ignores possible influences of terrain, fetch, and swell. The computational domain of the wave model is sufficiently large with 1000 km × 1000 km. Such a large wave domain is chosen to eliminate fetch dependence on wave development. Sensitivity experiments with smaller wave model domains indicate that our major conclusions are not sensitive to details of the wave model domain size, provided that fetches are sufficiently long so that waves can sufficiently develop, as they do in common open ocean conditions. Furthermore, a direct comparison with field observations suggests that wave simulations based on our domain size adequately capture many observed features of developing two-dimensional wave height spectra (Fig. 2).

Wave model results are used at a center location ($x = 500$ km, $y = 500$ km) that is not affected by the domain boundary. The wave spectrum is discretized into 48 evenly spaced directions with $\Delta\theta = 7.5°$, and 41 logarithmically spaced frequencies F ranging from 0.0418 to 2 Hz with $\Delta F = 0.1F$. This research employs the default SWAN settings of wave physics and boundary conditions, except that we change the value of wave steepness to 6.02×10^{-3} for a better agreement with observed wave spectra (Donelan et al. 1985). A stationary wave field is first established under the constant northward wind before the wind turns. Stationary SWAN results are consistent with typically observed wind-driven equilibrium wave height spectra (Donelan et al. 1985; Booij et al. 1997).

Several previous studies have analyzed the directional response of waves under abruptly turning winds based on observations and numerical models (Holthuijsen et al. 1987; Young et al. 1987; van Vledder and Holthuijsen 1993). Observations indicate that the direction of the waves adjusts to the new wind direction, and that shorter waves respond faster. Young et al. (1987) show that young waves, which propagate along the new wind direction, develop approximately independently of wind-misaligned older waves, which gradually decay due to wave dissipation.

To test our approach, we compare our wave simulations with the observations from Fig. 1. Observations are from the buoy data of the National Data Buoy Center (NDBC) buoy 41002, which is located in the Atlantic Ocean about 420 km south off Cape Hatteras and provides meteorological data every 10 min and wave data each hour. Consistent with the idealized experiments, observed wind speeds are roughly constant from 0000 UTC 5 March to 0200 UTC 7 March 2015, and observed wind directions abruptly change from northeast to south by about 120° at 0900 UTC 6 March (Fig. 1). The SWAN model, which is driven by the observed winds, successfully captures the directional response of the observed wave height spectrum (Fig. 2). In particular, high-frequency waves adjust more quickly than low-frequency ones, consistent with previous studies (van Vledder and Holthuijsen 1993; Young and Verhagen 1996). The agreement of wave model results with observations and previous studies suggests that our wave model approach is adequate to investigate transient, developing wave effects on OSBL turbulence.
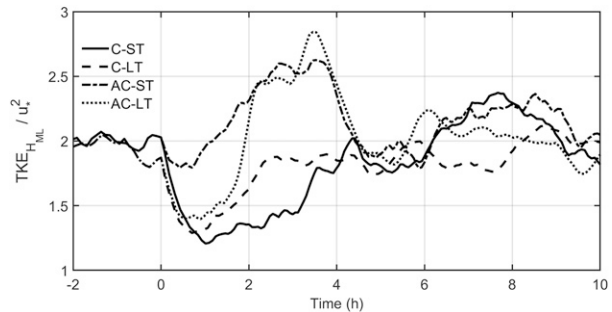

FIG. 3. Time series of normalized bulk TKE for C-ST (solid line), C-LT (dashed line), AC-ST (dash–dotted line), and AC-LT (dotted line).

3. Results

a. Overview of transient depth-averaged TKE

First, the bulk TKE of the four experiments (Table 1) are examined to study the turbulent response to the sudden change of wind direction (Fig. 3).

$$\text{TKE}_{H_{\text{ML}}} = \frac{1}{H_{\text{ML}}} \int_{-H_{\text{ML}}}^{0} \langle u_i' u_i' \rangle / 2 \, dz, \qquad (9)$$

where the subscript H_{ML} indicates averaging the value from $z = 0$ to $z = -H_{\text{ML}}$; H_{ML} is the initial mixed layer depth defined as the depth of the largest temperature gradient (Harcourt and D'Asaro 2008), which is approximately constant in this study. After the wind turns, the bulk TKE of all cases first weakens during stage 1 and then strengthens during stage 2. During stage 3, the bulk TKE does not change significantly. Turbulence becomes fully developed but still adjusts because of the slowly developing wave field in the LT cases.

Both waves (ST/LT) and the turning direction of the wind [cyclonic (C)/anticyclonic (AC)] affect the responses of OSBL turbulence. The bulk TKE weakens more for the C cases, especially for C-ST. Unexpectedly, for the AC cases, TKE levels exceed those found for constant winds, which we refer to as TKE overshoot. Those TKE variations indicate that TKE does not scale with u_*^2 under the sudden change of wind direction, so that the OSBL is not in equilibrium with the wind forcing. For LT, the transient OSBL response is also due to more slowly developing waves.

A conceptual sketch summarizes intuitively the OSBL turbulence response to abruptly turning winds with the characteristic stages 1–3, which are expected to depend not only on time but also on depth (Fig. 4). To understand the transient process, this paper first focuses on the relatively straightforward nonresonant C-ST case (section 3b). We then explore how LT modifies the OSBL response to cyclonically turning winds (section 3c). Last, the AC cases and the differences between the C and AC cases are discussed in section 3d.

b. OSBL response for C-ST case

1) TKE BUDGETS

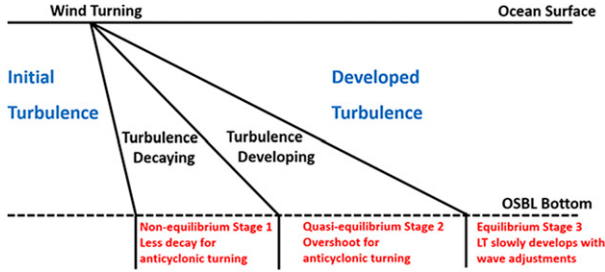The TKE budget equation is introduced to investigate the OSBL turbulence response,

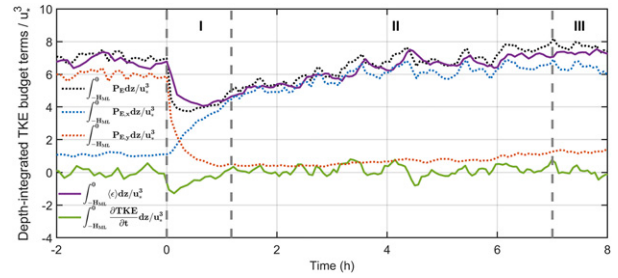FIG. 4. Conceptual sketch of the OSBL response to abruptly turning winds.

FIG. 5. Time series of normalized mixed layer–integrated TKE budget terms for C-ST. The wind direction suddenly changes from north to west at $t = 0$. Different lines represent the time series of normalized mixed layer–integrated TKE Eulerian shear production P_E (dotted lines, where the black line is the total contribution, the blue line is the along-wind contribution, and the red line is the crosswind contribution), dissipation rate (purple line), and TKE temporal rate of change (green line). Vertical gray dashed lines divide the time series into three stages on the basis of the mixed layer–integrated TKE budgets.

$$\frac{\partial \langle \tilde{u}_i' \tilde{u}_i' \rangle / 2}{\partial t} = -\langle \tilde{w}' \tilde{u}_i' \rangle \frac{\partial \langle \tilde{u}_i \rangle}{\partial z} - \langle \tilde{w}' \tilde{u}_i' \rangle \frac{\partial u_{s,i}}{\partial z} - \frac{g_i}{\rho_0} \langle \tilde{w}' \tilde{\rho}' \rangle$$

$$- \frac{\partial}{\partial z} \left(\frac{1}{2} \langle \tilde{u}_i' \tilde{u}_i' \tilde{w}' \rangle + \frac{1}{\rho_0} \langle \tilde{u}' \tilde{p}' \rangle \right) - \langle \epsilon \rangle + \text{SGS}, \quad (10)$$

where $\langle \tilde{u}_i \rangle$ is equal to $\langle u_i \rangle$. The left-hand side of Eq. (10) represents the temporal rate of change of resolved TKE. The right-hand side terms are TKE production from Eulerian shear P_E (first term), TKE production from Stokes drift shear P_S (second term), buoyancy flux (third term), vertical divergence of TKE vertical transport due to turbulence and pressure work (fourth term), TKE dissipation rate (fifth term), and all remaining subgrid-scale terms SGS (last term; Skyllingstad et al. 2000).

To obtain the bulk TKE budget, Eq. (10) is depth-integrated from $z = -H_{\text{ML}}$ to $z = 0$. Production P_S is zero for the case without wave forcing. The buoyancy term is much smaller than the major terms in our cases without strong entrainment. For our well resolved LES, the depth-integrated TKE budget equation for ST is approximately

$$\int_{-H_{\text{ML}}}^{0} \frac{\partial \langle \tilde{u}_i' \tilde{u}_i' \rangle / 2}{\partial t} \, dz \approx \int_{-H_{\text{ML}}}^{0} P_E \, dz - \int_{-H_{\text{ML}}}^{0} \langle \epsilon \rangle \, dz. \quad (11)$$

The depth-integrated P_E rapidly reduces and does not balance the depth-integrated dissipation during stage 1. Hence, the turbulence is not in equilibrium, so that production and dissipation are not balanced, leading to the decrease of TKE (Fig. 5). During stage 2, the depth-integrated P_E slightly exceeds the depth-integrated dissipation resulting in the increase of TKE, which approaches its value for fully developed OSBL. The relatively slow change of TKE suggests that OSBL turbulence is nearly in equilibrium (quasi-equilibrium) for stage 2. During stage 3, turbulence is in equilibrium and reaches its fully developed states.

Hereinafter, along-wind and crosswind refer to the new wind directions after the wind turns. For simplicity, the TKE production due to the along-wind shear and stress is called along-wind production, and the production due to the crosswind shear and stress is called crosswind production. Just after the wind turns, TKE is mainly produced by crosswind contributions, consistent with the old wind direction. Then, the major contribution of production changes from the crosswind component to the along-wind component (Fig. 5). The different changing rates of the shear production components cause the

variation of the total shear production and change the bulk TKE. The mechanism of the change of the production components will be examined next.

2) EVOLUTION OF VERTICAL PROFILES

The large initial crosswind velocity shear cannot be maintained after the wind turns (Fig. 6d), further weakening the turbulent stress and resulting in the decrease of crosswind shear production. At the same time, the wind stress accelerates along-wind near-surface currents to strengthen the velocity shear and turbulent stress, leading to an increase of along-wind shear production.

In addition to the TKE, the vertical velocity variance w_{rms}^2 is an important indicator for turbulent mixing in the OSBL. The TKE and w_{rms}^2 responses to the turning wind are faster at shallower depths in the OSBL (Figs. 6a,b), because those depths are more directly exposed to the wind forcing and smaller turbulent eddies respond faster. Initially, the mean Eulerian currents are less responsive and continue to provide a source of TKE (Figs. 6c,d). At the same time, near-surface along-wind currents accelerate more quickly to generate TKE-producing shear instabilities. A simple ST model is introduced subsequently to better understand the time scales of turbulent adjustment.

3) COMPARISON OF RANS MODELS

The RANS model results based on the KPP and SMC turbulent closure models compare well with the LES results (Fig. 7). Both components of velocity shear change fastest at the beginning and then slowly converge to a stationary state with time. The minimum total TKE productions of the KPP and SMC models approximately coincide with the LES results. The SMC results show that the along-wind velocity shear and P_E are characterized by a small overshoot (Figs. 7c,i), which is not present in the KPP results (Figs. 7b,h). These differences are in part due to the KPP turbulence equilibrium assumption that scales a turbulent velocity with the instantaneous wind and
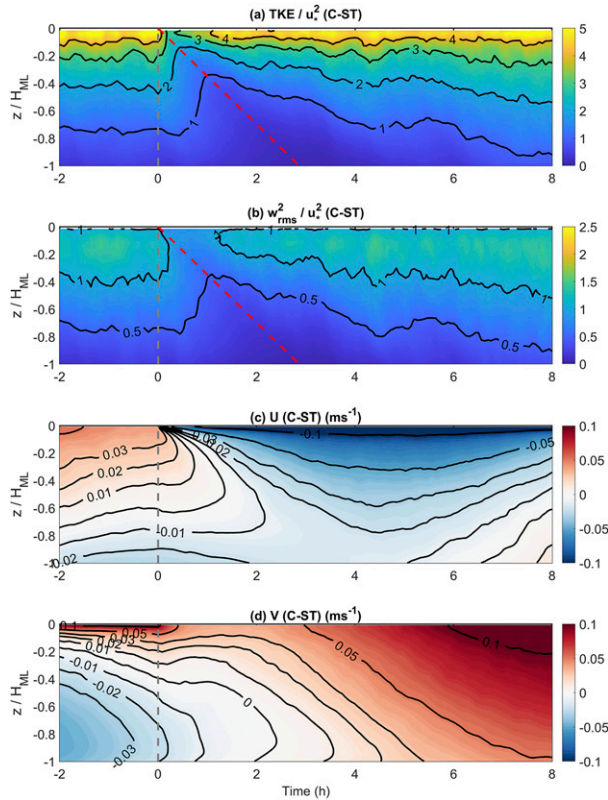
FIG. 6. Time series of horizontally averaged (a) normalized TKE, (b) normalized $\langle w_{rms}^2 \rangle$, and (c) along-wind and (d) crosswind Eulerian velocity profiles for C-ST. The red line in (a) and (b) is $z_m = -\ln(2)\kappa u_* t$, an estimated depth related to the time of minimum TKE production on the basis of a simplified ST model (section 3b). The wind direction turns at $t = 0$ h (vertical dashed gray line).

wave forcing, which is a nontrivial assumption for transient turbulence. This will be further investigated in section 3d.

Motivated by the success of the KPP model, we introduce a simpler model to gain further insights into the TKE evolution and specifically into the time scales of the turbulence decay, which separate OSBL response stages 1 and 2. To make analytical progress, we assume an eddy viscosity consistent with solid wall boundary layers $\nu_e(z) = -\kappa u_* z$, where $\kappa = 0.4$ is the von Kármán constant. For short times $t < -z/(fd)$, where d is the depth scale of the Ekman layer under stationary condition, the Coriolis force is negligible (e.g., Lewis and Belcher 2004) and will not be included in the following analysis. We set the along-wind initial condition to zero and the crosswind flow to the analytical solution of the simple model under the northward wind forcing. Using Laplace transforms (Madsen 1977; Lewis and Belcher 2004), the solutions for the along-wind and crosswind velocity shear can be determined, respectively, as

$$\frac{\partial \langle u \rangle}{\partial z} = \frac{u_*}{\kappa z} e^{z/(\kappa u_* t)} \quad \text{and} \tag{12}$$

$$\frac{\partial \langle v \rangle}{\partial z} = -\frac{u_*}{\kappa z} \left[1 - e^{z/(\kappa u_* t)}\right], \tag{13}$$

where $-u_*/(\kappa z)$ represents the magnitude of stationary velocity shear, which is dependent on depth and friction velocity. The signs of Eqs. (12) and (13) indicate the vector direction. The exponential term $e^{z/(\kappa u_* t)}$ controls the change rate of velocity shear and depends on depth, friction velocity, and time. These analytical velocity shears agree well with LES and KPP results (Figs. 7a,b,d,e). The changing rates of velocity shears are largest initially near the surface and then decrease with time and depths. The magnitudes of those changing rates are also the same for both components. Based on the analytical solution of velocity shear and the turbulent stress given by Eq. (4), the along-wind, crosswind, and total P_E are, respectively,

$$P_{E,x} = -\frac{u_*^3}{\kappa z} e^{2z/(\kappa u_* t)}, \tag{14}$$

$$P_{E,y} = -\frac{u_*^3}{\kappa z} \left[1 - e^{z/(\kappa u_* t)}\right]^2, \quad \text{and} \tag{15}$$

$$P_E = -\frac{u_*^3}{\kappa z} \left\{ e^{2z/(\kappa u_* t)} + \left[1 - e^{z/(\kappa u_* t)}\right]^2 \right\}. \tag{16}$$

These solutions show that P_E adjusts more quickly at shallower depths. These solutions also reveal the different changing rates of TKE production for the along-wind and crosswind contributions, consistent with LES and KPP results (Fig. 7). The idealized model suggests that the time of minimum TKE production is related to depth as $z_m = -\ln(2)\kappa u_* t$, which coincides with the LES results of minimum TKE and w_{rms}^2 (Figs. 6a,b). The alignment of minimum TKE and w_{rms}^2 with minimum TKE production is not trivial and suggests that terms in the TKE and velocity variance balances rapidly adjust. Note also that w_{rms}^2 is not directly produced by mean shear but is transferred through pressure terms from horizontal TKE (see, e.g., Kantha and Clayson 1994) whose x and y production components change here at different rates.

c. OSBL response for C-LT

The previous section indicates that the sudden change of wind direction causes substantial variability in ST. Here, we examine the more complex, yet more realistic OSBL response to turning winds in the presence of evolving LT. A key difference between the LT and ST cases is that the waves also adjust after the wind turns. Wave model results indicate that the adjustment of the Stokes drift significantly depends on depth (Fig. 8). Because high-frequency waves adjust faster than low-frequency waves, the Stokes drift near the surface responds more quickly according to Eq. (2). The different time scales lead to the misalignment of wind and waves, which further influences the OSBL response.

1) MIXED LAYER–INTEGRATED w_{rms}^2 AND TKE BUDGETS

One important indicator for the presence of LT is enhanced w_{rms}^2 (McWilliams et al. 1997; D'Asaro 2001). The mixed layer–integrated bulk w_{rms}^2 is also used for scaling LT. McWilliams et al. (1997) introduce the turbulent Langmuir number $La_t = (u_*/u_{s0})^{1/2}$ to describe the relative importance of LT and ST, where u_{s0} is the magnitude of surface Stokes drift in the
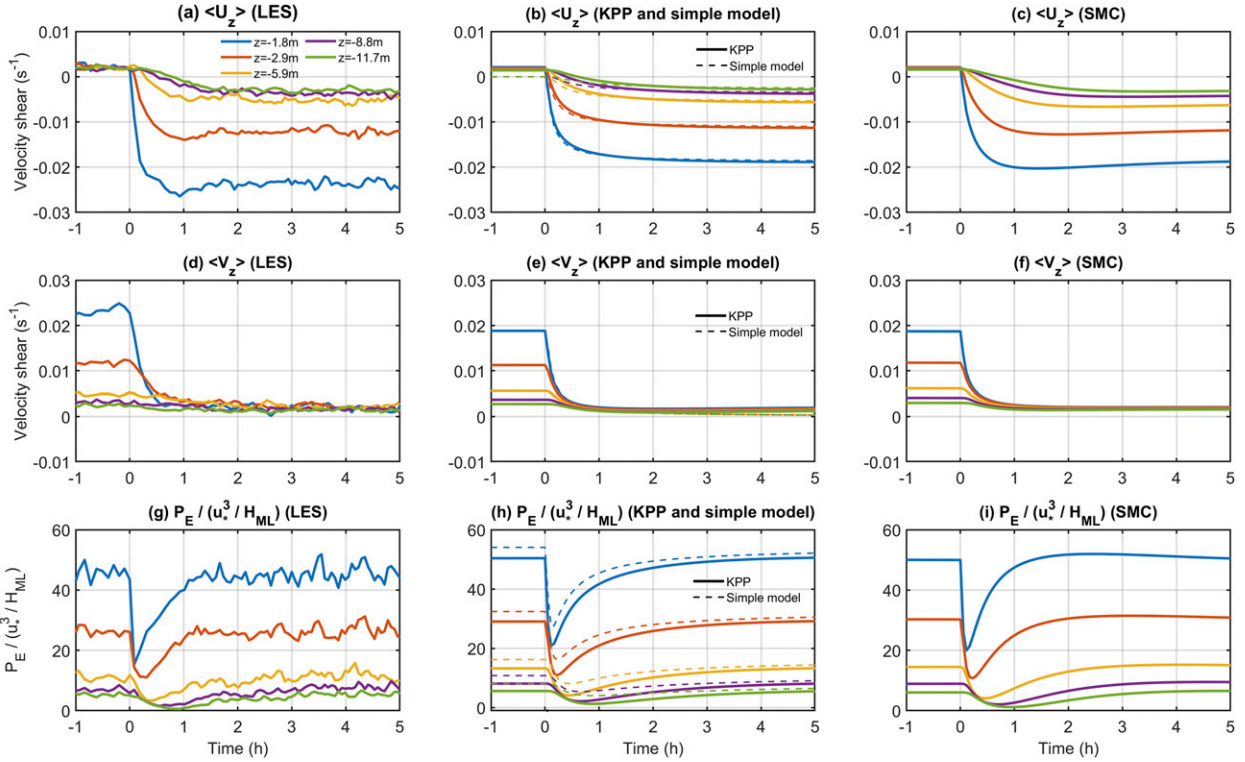
FIG. 7. Results of (left) LES, (center) KPP (solid lines) and simple model (dashed lines), and (right) SMC for C-ST (a)–(c) along-wind Eulerian velocity shear, (d)–(f) crosswind Eulerian velocity shear, and (g)–(i) normalized Eulerian shear production P_E. The lines with different colors represent the time series of values at specific depths, as labeled in (a).

direction of wind stress. LES results show that LT dominates when $\mathrm{La}_t < 0.7$ (Li et al. 2005; Belcher et al. 2012). However, the OSBL averaged vertical velocity variance also significantly depends on the Stokes drift's vertical decay (Harcourt and D'Asaro 2008; Kukulka and Harcourt 2017). Harcourt and D'Asaro (2008) define a surface layer Langmuir number $\mathrm{La}_{\mathrm{SL}}$ to capture the wavelength dependence of LT for both monochromatic and broadband wave spectra,

$$\mathrm{La}_{\mathrm{SL}} = \sqrt{\frac{u_*}{|\mathbf{u}_s^{\mathrm{SL}} - \mathbf{u}_s(z_{\mathrm{ref}})|}}, \qquad (17)$$

where $\mathbf{u}_s^{\mathrm{SL}}$ is the Stokes drift vector averaged over surface layer defined as the top 20% of the OSBL, and $\mathbf{u}_s(z_{\mathrm{ref}})$ is a reference Stokes drift vector evaluated at depth z_{ref} (Harcourt and D'Asaro 2008). For misaligned wind and waves, Van Roekel et al. (2012) introduce the projected surface layer Langmuir number $\mathrm{La}_{\mathrm{SL}}^{\mathrm{Proj}}$ for LT scaling,

$$\mathrm{La}_{\mathrm{SL}}^{\mathrm{Proj}} = \sqrt{\frac{u_* \cos(\alpha_{\mathcal{L}})}{|\mathbf{u}_s^{\mathrm{SL}} \cos(\theta_{ww} - \alpha_{\mathcal{L}})|}}, \qquad (18)$$

where $\alpha_{\mathcal{L}}$ is the direction of depth-averaged Lagrangian velocity shear over the surface layer and θ_{ww} is the angle between wind and surface Stokes drift $\mathbf{u}_s(0)$.

We compare the bulk w_{rms}^2 with previous empirical LT scaling relations for constant wind and wave forcing (Fig. 9a).

After the wind turns, bulk w_{rms}^2 experiences three stages, consistent with the TKE result in Fig. 3. The bulk w_{rms}^2 that is based on $\mathrm{La}_{\mathrm{SL}}^{\mathrm{Proj}}$ varies more significantly than the estimate that is based on $\mathrm{La}_{\mathrm{SL}}$ and is closer to the LES results, which indicates that both changing Stokes drift magnitude and wind-misalignment influences LT. The deviations of LES results from scaling relations developed for equilibrium wind and waves indicate that the OSBL turbulence is not fully equilibrated with the wind and wave forcing, so that turbulence develops and is nonstationary.
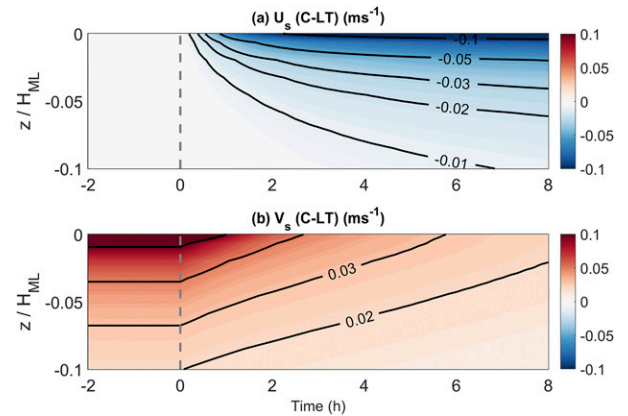

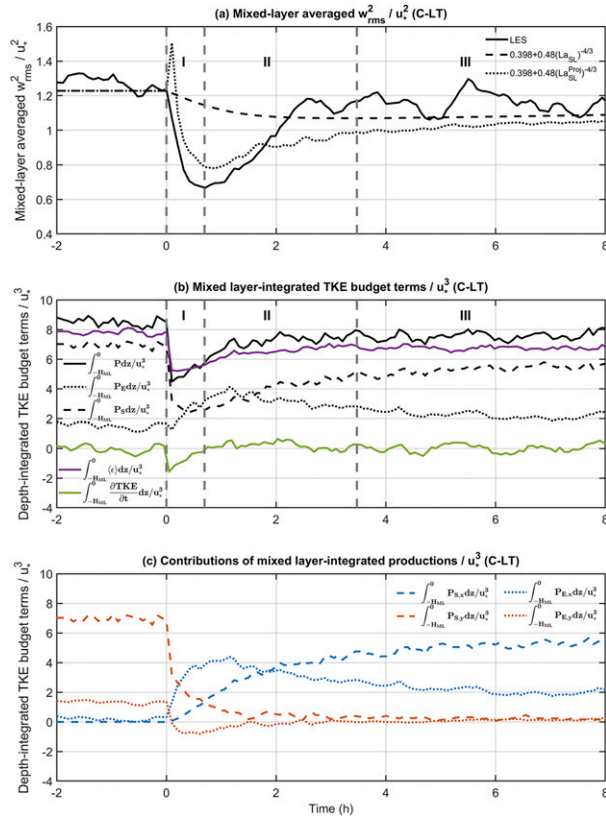FIG. 8. Time series of (a) along-wind and (b) crosswind Stokes drift profile for C-LT.

FIG. 9. (a) Time series of the bulk w_{rms}^2 for C-LT: LES results (solid line) and empirical scaling results on the basis of La_{SL} (dashed line) and La_{SL}^{Proj} (dotted line). (b) Time series of normalized mixed layer–integrated total production P (black solid line), total Eulerian shear production P_E (black dotted line), total Stokes production P_S (black dashed line), dissipation rate ϵ (purple line), and TKE temporal rate of change (green line). (c) Time series of normalized along-wind (blue lines) and crosswind (red lines) contributions of mixed layer–integrated P_E (dotted line) and P_S (dashed line). Vertical gray dashed lines divide the time series into three stages on the basis of the mixed layer–integrated TKE budgets.

During the adjustment process, both P_E and P_S can be dominant, and their relative importance changes (Figs. 9b,c). The P_S is most important when wind and waves are aligned, exceeding P_E by a factor of 3–4 consistent with earlier work (McWilliams et al. 1997). Just after the wind turns, TKE production is mainly due to contributions from the old wind direction, alike the ST case (Fig. 9c). The slow adjustment of waves initially leads to a near-perpendicular misalignment between the Stokes drift and wind, resulting in weak P_S consistent with previous studies (Van Roekel et al. 2012; Sullivan et al. 2012; Rabe et al. 2015). Furthermore, a near-surface Eulerian flow that opposes the Stokes drift develops, which is called the anti-Stokes flow (Pearson 2018). Therefore, the OSBL turbulence response is expected to be more complex in the LT cases.

The rapidly formed along-wind Eulerian current (Fig. 10c) leads to enhanced along-wind P_E, which develops fast and
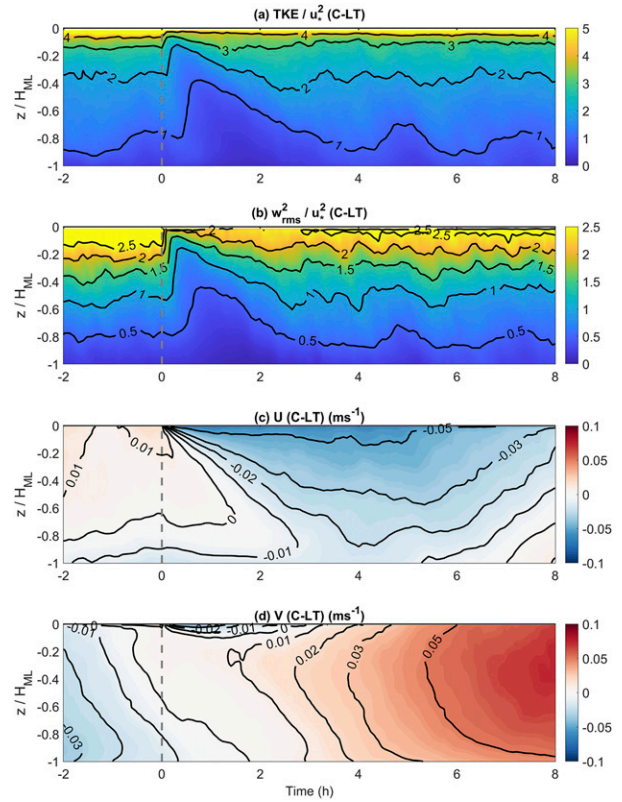

FIG. 10. Time series of horizontally averaged (a) normalized TKE, (b) normalized $\langle w_{rms}^2 \rangle$, and (c) along-wind and (d) crosswind Eulerian velocity profiles for C-LT.

penetrates with depth after the wind turns (Fig. 11a). Meanwhile, the anti-Stokes flow also rapidly develops and balances the still significant crosswind Stokes drift (Fig. 10d), further weakening the crosswind Lagrangian velocity shear to generate negative crosswind P_E that partially balances P_S (Fig. 11b). Most of P_S concentrates at the depth above $0.2 H_{ML}$ because of the quickly decaying Stokes drift. The dynamics driving the turbulent response are greatly different despite the similarity of total TKE variations for ST and LT (Figs. 10a,b). The decline of production for LT is due to the decreased P_S and the negative crosswind P_E caused by the anti-Stokes flow. After the wind turns, the Lagrangian velocity shear adjusts to the new wind direction near the surface due to the rapid development of the Eulerian currents. Because of the misalignment of wind and waves, P_E becomes comparable to and even exceeds P_S (Fig. 11c). Thus, OSBL turbulence initially transitions from LT to ST after the wind turns. Eventually, the Stokes drift gradually aligns with the new wind, leading to the recovery of P_S and the reduction of P_E as LT enhances mixing to reduce shear. During this time, the turbulence transitions from ST to LT, which is consistent with the reduction of La_{SL}^{Proj} and associated with the strengthening of LT, characterizing stage 3. During this stage, the turbulence is nearly fully developed and only slowly grows as a result of the slow adjustment of waves, while the
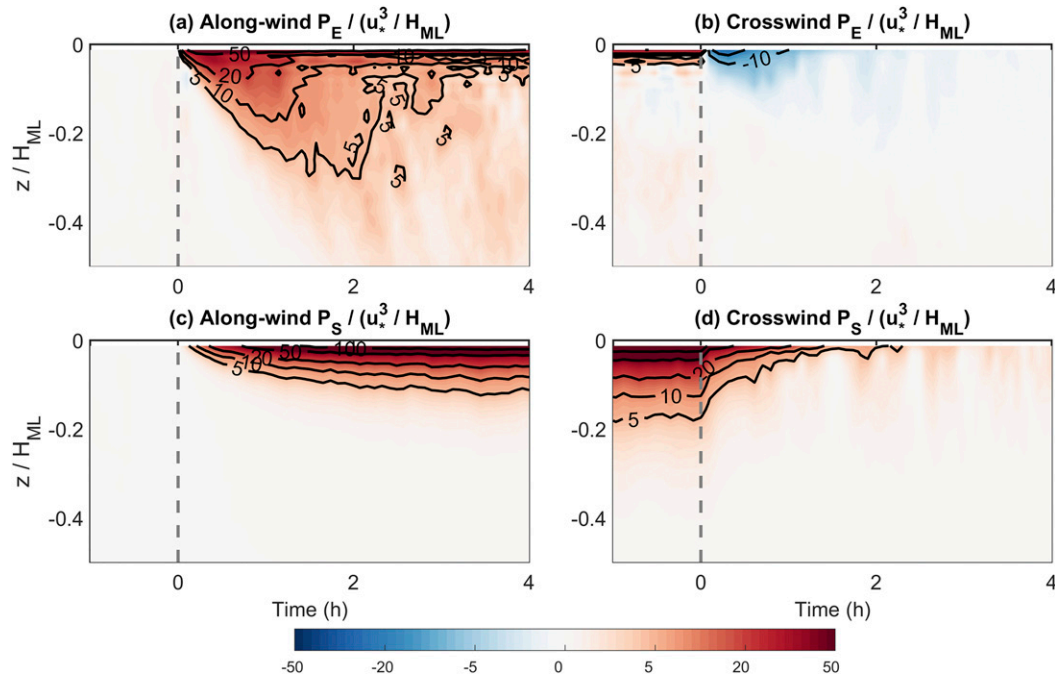
FIG. 11. Time series of normalized (left) along-wind and (right) crosswind profiles of (a),(b) P_E and (c),(d) P_S for C-LT.

turbulence of OSBL is approximately equilibrated with the wind and wave forcing.

2) DEVELOPING LT AND LC

Figure 12 shows snapshots of the cross sections of normalized vertical velocity w/u_* at the depth close to the maximum vertical velocity variance $z = -2.9$ m. The adjustment of LCs is rapid and happens within 2 h after the wind turns. The cross section at $t = 0$ s is for the stationary case under aligned wind and waves, with the largest magnitude of vertical velocity (Fig. 12a). After the wind turns, LCs turn into the direction of the wind stress, and their direction generally aligns with the direction of Lagrangian velocity shear (magenta arrows in Fig. 12), consistent with previous work (Van Roekel et al.
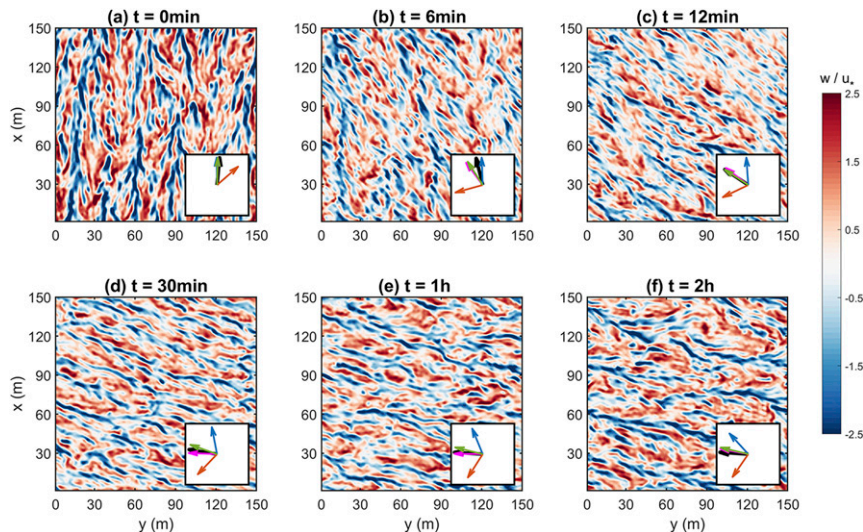

FIG. 12. Cross-sectional snapshots of normalized vertical velocity w/u_* at the depth of maximum vertical velocity variance $z = -2.9$ m in the C-LT case. Arrows show the directions of Stokes drift shear (blue), Eulerian velocity shear (orange), Lagrangian velocity shear (magenta), turbulent stress (black), and Langmuir cells (green) at this depth.
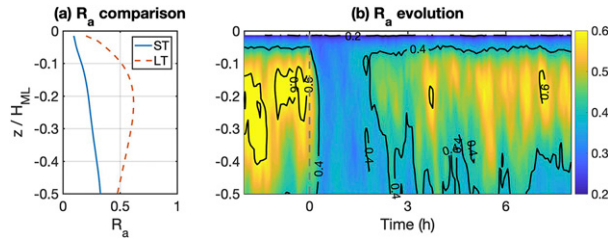
FIG. 13. (a) Initial stationary anisotropy ratio R_a for ST (solid line) and LT (dashed line). (b) Time series of the profile of R_a for C-LT.

2012). The identification of the LCs direction (green arrows in Fig. 12) is based on the velocity autocorrelations following previous studies (Sullivan et al. 2012; Wang et al. 2019). As the magnitude of the vertical velocity weakens, the windrows become less coherent (Figs. 12b,c). After 1 h, clearly identifiable windrows have developed that align with the Lagrangian velocity shear, consistent with expectations for stationary conditions (Van Roekel et al. 2012). The turbulent stress (black arrows in Fig. 12) is generally aligned with the Lagrangian velocity shear during the adjustments, except shortly after the wind turns.

It is also interesting to examine whether the sudden wind turning influences LT over the entire depth range where downwelling flows are expected to be relatively strong due to

LT. We use a dimensionless index, velocity variance anisotropy ratio R_a (Polton and Belcher 2007; Rabe et al. 2015), to determine the strength of the LT,

$$R_a = \frac{\langle w'^2 \rangle}{\langle u'^2 \rangle + \langle v'^2 \rangle}. \tag{19}$$

Consistent with earlier studies (Rabe et al. 2015; Wang et al. 2019), we find that R_a is larger with than without LT at the depth above $0.5H_{ML}$ with a value exceeding 0.4 for constant forcing (Fig. 13a). After the wind turns, R_a quickly decreases for about 2 h indicating weak LT (Fig. 13b). Ratio R_a then slowly increases to the value for the fully developed state. The slow adjustment of R_a is consistent with the developing wave field. The vertical profile of the evolution of R_a indicates that the strength of Langmuir turbulence in the entire OSBL decreases as turbulence weakens.

3) STRESS BUDGETS AND LIMITATIONS OF RANS MODEL INCLUDING LT

The evolution of the LES velocity shear for LT (Figs. 14a,b) shows that the Eulerian velocity shear dominates the Lagrangian velocity shear during a short time after the wind turns. Moreover, the crosswind Lagrangian velocity shear develops more slowly than the along-wind shear, unlike the ST LES results (Fig. 7).

We first apply the KPP-LT model (Reichl et al. 2016) to study the LT response. The KPP-LT model roughly captures
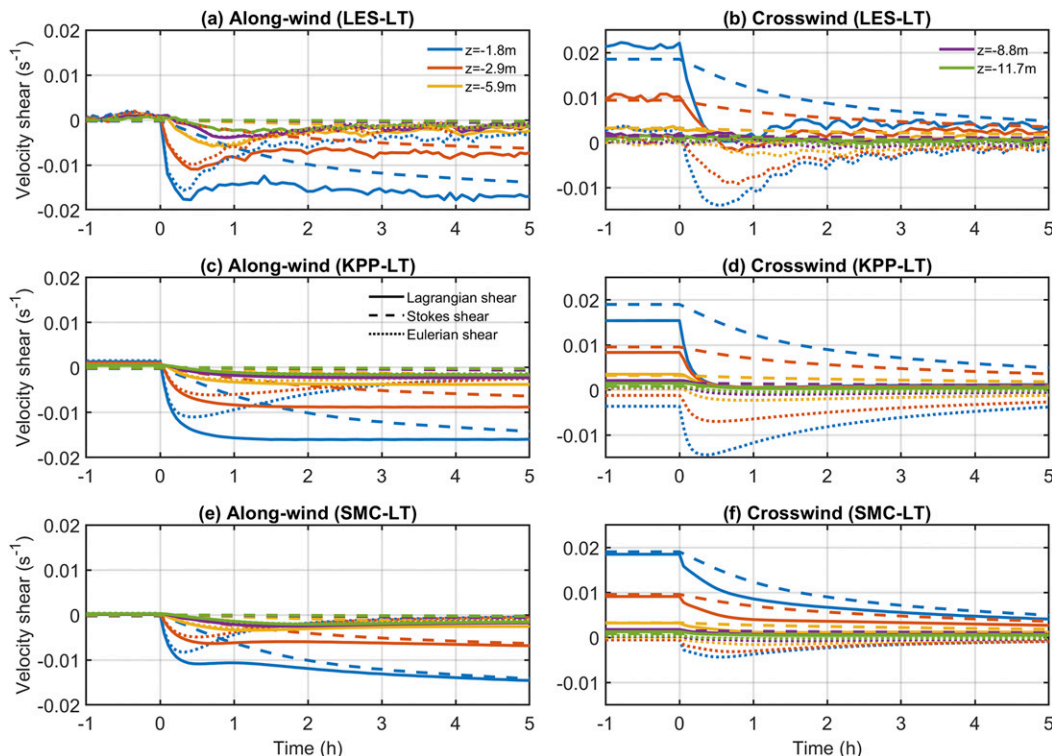

FIG. 14. Time series of (left) along-wind and (right) crosswind Lagrangian velocity shear (solid line), Stokes drift shear (dashed line), and Eulerian velocity shear (dotted line) for (a),(b) LES; (c),(d) KPP-LT; and (e),(f) SMC-LT for cyclonically turning winds. Lines with different colors represent different depths, as labeled in (a).
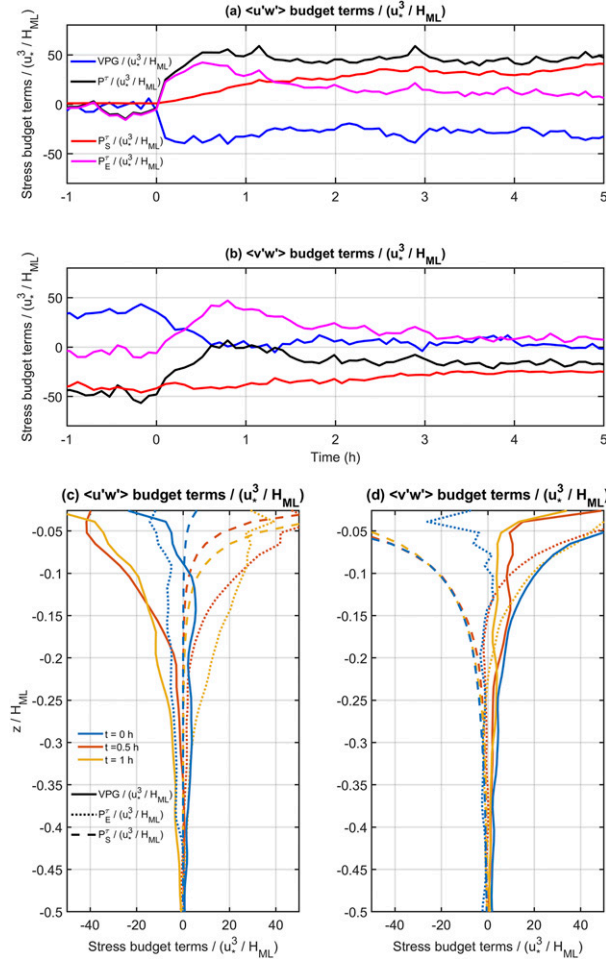
FIG. 15. Time series of normalized (a) along-wind and (b) cross-wind turbulent stress budget terms at $z = -1.8$ m for C-LT, including contributions from Eulerian shear P_E^τ (magenta line), Stokes drift shear P_S^τ (red line), Lagrangian velocity shear P^τ (black line), and pressure strain rate (VPG; blue line). Also shown are the transient profiles of normalized (c) along-wind and (d) crosswind turbulent stress budget terms, including VPG (solid line), P_E^τ (dotted line), and P_S^τ (dashed line).

Eulerian shear trends with similar magnitudes (Figs. 14c,d). However, the crosswind and along-wind Eulerian shears from the KPP-LT model adjust at a rate similar to the ST case (Figs. 14c,d), which is inconsistent with the LT LES results.

To examine these different response rates, the turbulent stress budget equation with the impact of the CL vortex force (Harcourt 2013) is next investigated. The resolved vertical fluxes of horizontal momentum $\langle \tilde{u}'\tilde{w}' \rangle$ and $\langle \tilde{v}'\tilde{w}' \rangle$ components evolve according to

$$\frac{\partial \langle \tilde{u}'\tilde{w}' \rangle}{\partial t} = -\langle \tilde{w}'\tilde{w}' \rangle \frac{\partial \langle \tilde{u} \rangle}{\partial z} - \left(\langle \tilde{u}'\tilde{u}' \rangle \frac{\partial u_s}{\partial z} + \langle \tilde{u}'\tilde{v}' \rangle \frac{\partial v_s}{\partial z} \right) - \left(\left\langle \tilde{u}' \frac{\partial \tilde{p}'}{\partial z} \right\rangle + \left\langle \tilde{w}' \frac{\partial \tilde{p}'}{\partial x} \right\rangle \right) + D_{13} \qquad (20)$$
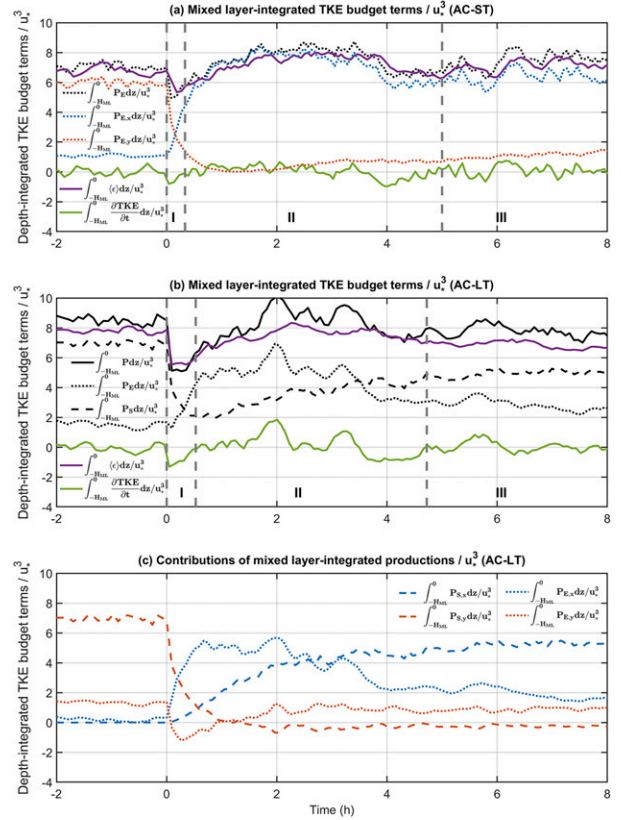

FIG. 16. (a) Time series of normalized mixed layer–integrated TKE budget terms for AC-ST. The representations of line styles and colors are the same as in Fig. 5. Also shown are time series of normalized mixed layer–integrated (b) TKE budget terms and (c) TKE production terms. The terms and line styles are the same as in Figs. 9b and 9c. Vertical gray dashed lines divide the time series into three stages on the basis of the mixed layer–integrated TKE budgets.

and

$$\frac{\partial \langle \tilde{v}'\tilde{w}' \rangle}{\partial t} = -\langle \tilde{w}'\tilde{w}' \rangle \frac{\partial \langle \tilde{v} \rangle}{\partial z} - \left(\langle \tilde{v}'\tilde{v}' \rangle \frac{\partial v_s}{\partial z} + \langle \tilde{u}'\tilde{v}' \rangle \frac{\partial u_s}{\partial z} \right) - \left(\left\langle \tilde{v}' \frac{\partial \tilde{p}'}{\partial z} \right\rangle + \left\langle \tilde{w}' \frac{\partial \tilde{p}'}{\partial y} \right\rangle \right) + D_{23}, \qquad (21)$$

where the left-hand sides are the time derivative of turbulent stress. The first two terms on the right-hand sides are the productions of turbulent stress from Eulerian velocity shear P_E^τ and Stokes velocity shear P_S^τ. The third term is the velocity pressure gradient term (VPG), and D_{i3} contains small terms related to buoyancy, Coriolis force, advection, dissipation, transport and subgrid scales.

A specific depth with strong Stokes drift is chosen to track the response of turbulent stress budgets after wind turning (Figs. 15a,b). Initially, P_S^τ is approximately balanced by VPG in the y direction (Fig. 15d). After the wind turns, the crosswind P_S^τ is still substantial; however, P_E^τ increases due to developing Eulerian shear (discussed above) and opposes P_S^τ, leading to the decrement of stress
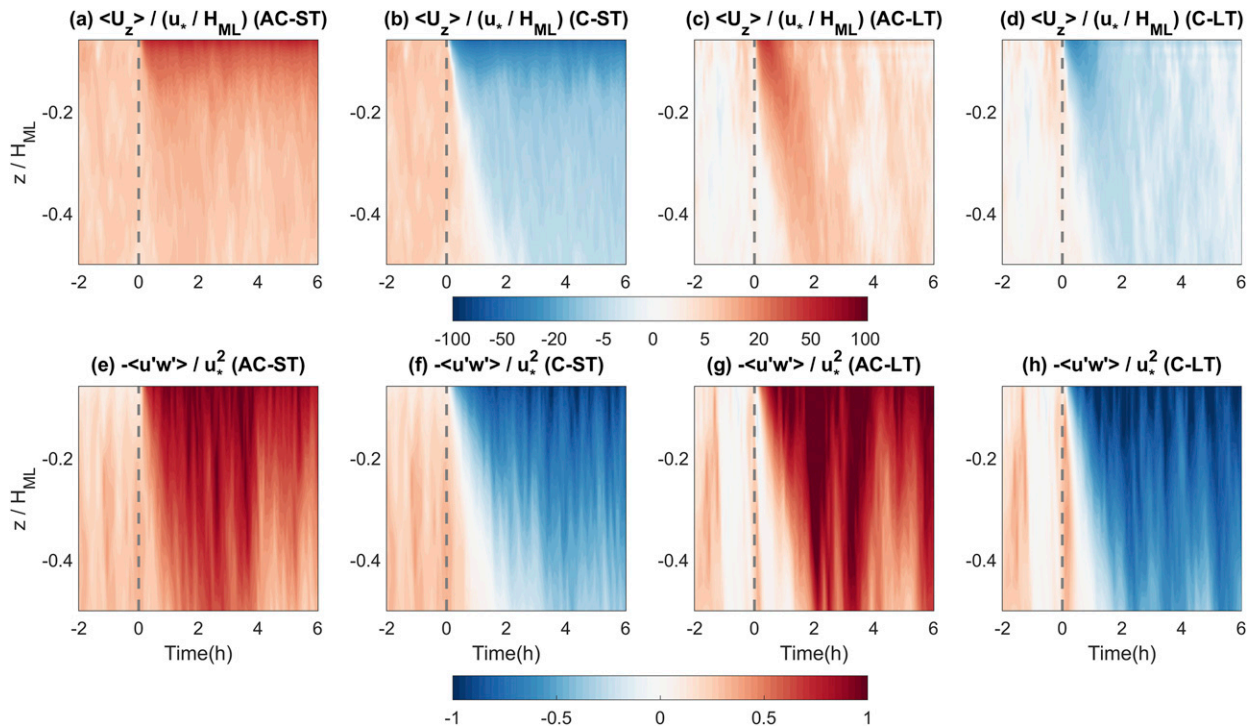
FIG. 17. Time series of normalized along-wind (a)–(d) Eulerian velocity shear profiles and (e)–(h) turbulent stress profiles for the (left) AC-ST, (left center) C-ST, (right center) AC-LT, and (right) C-LT cases.

production. In the along-wind direction, the slow adjustment of the Stokes drift leads to a small contribution of P_S^{τ}, and along-wind VPG is balanced by the along-wind P_E^{τ} (Fig. 15c). Because of the existence of the Stokes drift, the evolution of the turbulent stress in LT is distinct from that in ST, further leading to the difference of velocity shear development.

On the basis of the results of turbulent stress budgets, the relative importance of P_E^{τ} and P_S^{τ} is different for along-wind and crosswind components, and it changes for nonstationary conditions. The KPP-LT model cannot capture such complex stress dynamics because it is based on the Lagrangian current and, thus, does not fully take into account the complex interaction between Eulerian currents and waves. Accordingly, when applying the simple model described in section 3b(3) to the LT case by replacing the Eulerian velocity with Lagrangian velocity, the simple model cannot capture the LES results because it does not explicitly capture stress production by Stokes drift shear.

The SMC-LT model (Harcourt 2015) accounts for the CL vortex force production, based on the transport equations for the Reynolds stress. The SMC-LT results (Figs. 14d,e) reproduce the LES results with a greater changing rate of along-wind than crosswind Lagrangian velocity shear. However, the details of the velocity shears are different, probably due to the inaccurate parameterization of turbulent stress that is obtained in equilibrium conditions for moderately misaligned wind and waves. For example, just after the wind turns the main contributions of P_S occur close to the surface. This decreases the eddy viscosity applied to the Stokes drift shear in the Harcourt (2015) parameterizations, which were obtained for moderately

misaligned wind and waves [see Eqs. (29)–(35) in Harcourt 2015]. The differences of the KPP-LT and SMC-LT model results confirm that the Stokes drift plays a key role in the transient development of turbulent stress.

d. Faster turbulent responses and enhanced TKE in AC cases

Figure 3 shows two significant differences in the OSBL responses between the cyclonic (C) and anticyclonic (AC) wind turning cases. First, the AC cases have relatively weak TKE decay right after the wind turns (stage 1), especially for AC-ST. Second, the AC cases have TKE overshoots during stage 2 after a time comparable to the inertial time scale $1/f$. Apart from these two differences, the evolutions of bulk TKE in the AC cases are similar to those of the C cases. This section will discuss the possible reasons for those differences.

1) RELATIVELY SMALL TKE REDUCTION DURING STAGE 1

In the AC-ST case, P_E decreases quickly and then increases more rapidly due to the faster growth of along-wind P_E at stage 1 (Fig. 16a), compared to the C-ST case (Fig. 5). For the LT cases, the sum of P_E and P_S (Fig. 16b) in AC-LT also rebounds faster than the one in C-LT (Fig. 9b) due to the earlier increase of P_E. The difference of P_E between C-ST and AC-ST is more significant than the one between the C-LT and AC-LT, so that the difference of TKE weakening is more evident for the ST cases than for the LT cases. A possible reason for those different TKE reductions will be provided next.
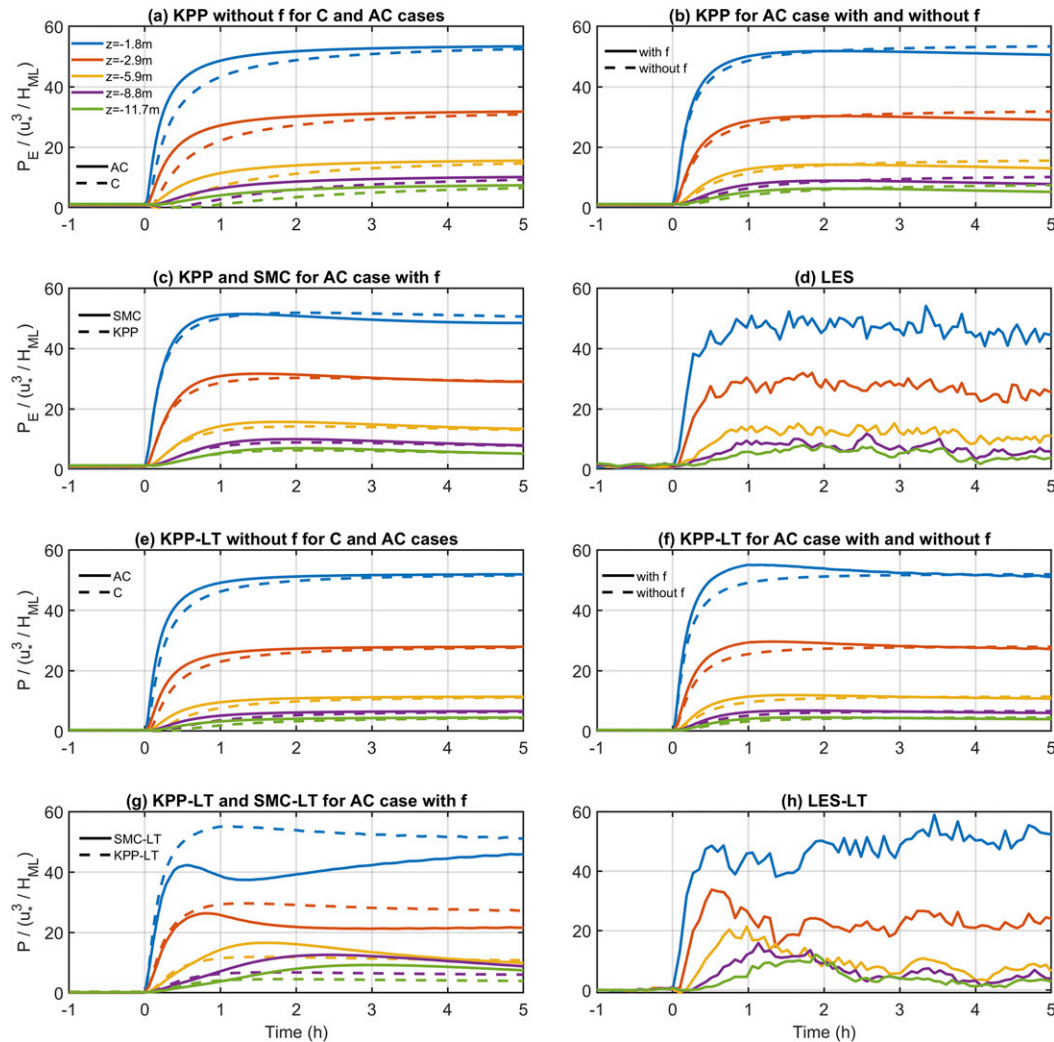
FIG. 18. Time series of normalized along-wind (top two rows) P_E without LT and (bottom two rows) P with LT for (a),(e) C (dashed line) and AC (solid line) without Coriolis force; (b),(f) AC with (solid line) and without (dashed line) Coriolis force; (c) KPP (dashed line) and SMC (solid line) and (g) KPP-LT model (dashed line) and SMC-LT model (solid line) results of AC with Coriolis force; and (d),(h) LES results of AC. Lines with different colors represent different depths, as labeled in (a).

Before the wind changes, the Ekman spiral includes Eulerian velocity shear in the east direction for Northern Hemisphere (Ekman 1905; Price et al. 1987). This preconditioned velocity shear is favorable for ST generation in the AC cases (wind turns eastward) but opposes the wind-driven shear for the C cases (Fig. 17). These different influences of initial shear lead to the different P_E evolution. After the wind turns, the along-wind P_E keeps increasing in AC-ST, while P_E first decreases to zero and then increases in C-ST. Consequently, ST is relatively strong for the AC-ST case but weak for the C-ST case during stage 1.

We employ the KPP model to examine this mechanism further. In these KPP experiments, the Coriolis force is omitted to focus on the influence of initial conditions. Indeed, KPP model results indicate that the along-wind P_E develops faster and reaches more quickly the final state for the AC-ST case (Fig. 18a).

Because of the enhanced mixing due to LT, the profile of Eulerian currents is more uniform, so that the initial along-wind Eulerian velocity shear is smaller (Fig. 17) and its initial along-wind P_E is almost zero. The small initial P_E does not substantially influence the shear production in the LT cases. Therefore, the differences between the AC and C cases are more pronounced in the ST case. Consistently, the KPP-LT models (Fig. 18e) show that the along-wind P_E in AC-LT still develops faster than the one in C-LT, but the differences are less pronounced.

2) TKE ENHANCEMENT FOR AC CASES DURING STAGE 2

The AC cases show TKE overshoots during stage 2 so that TKE levels exceed those of the fully developed state (Fig. 3). The TKE overshoot is caused by enhanced P_E (Fig. 16), which is

dominated by along-wind contributions. The analysis of the previous subsection indicates that the preconditioned velocity shear and turbulent stress can promote TKE development shortly after the wind turns anticyclonically. However, KPP models without Coriolis force cannot reproduce the enhanced P_E, which indicates the importance of the Coriolis force and inertial resonance (Fig. 18a). Here we focus on the development of along-wind production and discuss two possible reasons for the TKE overshoot.

The first reason is due to inertial resonance. The TKE overshoot appears after around three hours, comparable to $1/f$ (Fig. 3), which is a time scale of Ekman layer development (Pollard et al. 1973; Price and Sundermeyer 1999; Lewis and Belcher 2004). The along-wind RANS equation is used to clarify this process. After vertical differentiation, the x component of Eq. (3) becomes

$$\frac{\partial}{\partial t}\left(\frac{\partial \langle u \rangle}{\partial z}\right) = f\left(\frac{\partial \langle v \rangle}{\partial z} + \frac{\partial v_s}{\partial z}\right) - \frac{\partial^2 \langle u'w' \rangle}{\partial z^2}. \qquad (22)$$

When the turbulence is stationary before the wind turns, the left-hand side of Eq. (22) is zero, and the positive Coriolis term balances the negative second derivative of stress (SDS) close to the ocean surface. For the AC cases, the Coriolis term is negative to balance the SDS when turbulence adjusts to the final states. Because of the positive initial value, the Coriolis term contributes to the development of the along-wind shear before it becomes negative. Therefore, the Coriolis term resonantly works with SDS to promote the development of along-wind Eulerian velocity shear. For C cases, the negative right-hand side is favorable to promote the velocity shear growth. The positive initial Coriolis term generates the opposite effect to suppress the development of along-wind velocity shear and P_E. Note that we considered the Coriolis term as small in the previous subsection because the SDS is much larger than the Coriolis term shortly after the wind turns. In contrast, the Coriolis term is comparable to SDS during the TKE overshoot.

For ST, the comparison of the KPP model results with and without the Coriolis force confirms this resonance effect (Fig. 18b), only the case with Coriolis force displays an overshoot. The KPP-LT model also confirms the contribution of the Coriolis force to the TKE overshoot for LT cases (Fig. 18f). Note that the eddy viscosity of the ST KPP model is determined from u_* and does not change after the wind turns. The KPP-LT model includes LT mixing via an enhancement factor that depends on a turbulent Langmuir number, which changes slightly due to the wave adjustment. To be consistent with the ST cases and to focus on Coriolis force effects, we use the eddy viscosity of the stationary state and set it to a constant profile for these proof-of-concept simulations.

The second reason for the TKE overshoot is due to the initial weakening of turbulence during nonequilibrium conditions. The abruptly turning wind causes relatively weak TKE because the transient TKE production is unable to balance dissipation. In turn, less developed turbulence leads to reduced vertical turbulent momentum fluxes, so that near-surface currents, directly driven by wind stress, accelerate more quickly (Figs. 6c and 10c). Eventually, accelerated near-surface currents become unstable, driving relatively strong transient turbulence.

We compare the results from KPP (KPP-LT), SMC (SMC-LT), and LES to confirm the effects of the time-varying eddy viscosity on the TKE overshoot. After the wind turns, the SMC (Fig. 18c) and SMC-LT (Fig. 18g) models, which employ the time-dependent eddy viscosity, yield shear productions with a pronounced peak, unlike the KPP models. The SMC model results also agree at least qualitatively with LES results. This comparison of RANS models with LES results indicates the presence of nonequilibrium turbulence that contributes to enhanced along-wind shear production and the TKE overshoot. Note that the C cases also experience weak turbulence levels initially. However, the off-inertial resonance for C cases suppresses the development of stronger along-wind velocity shear and leads to a more gradual TKE development (Fig. 7).

4. Conclusions

In this study, we employ an LES approach to investigate the transient ocean surface boundary layer (OSBL) response to abruptly turning winds. Idealized experiments are designed with Langmuir turbulence (LT) and without LT (shear-driven turbulence or ST) for winds that abruptly turn by 90° either cyclonically (case C) or anticyclonically (case AC). LT is driven by the Craik–Leibovich vortex force whose transient Stokes drift is determined from spectral wave simulations. Complex three-dimensional LES results are also compared with two common turbulence closure models employed in Reynolds-averaged Navier–Stokes equation (RANS) models of the OSBL.

Our results suggest a three-stage depth-dependent response of the OSBL due to abruptly turning winds (Fig. 4). The OSBL response is depth-dependent because turbulence responds faster at shallower depth due to the direct exposure to the wind forcing and smaller turbulent eddies. During stage 1, turbulent kinetic energy (TKE) decreases and turbulence is not equilibrated with the wind or wave forcing, because relatively weak TKE production cannot balance TKE dissipation. For ST, the TKE reduction is due to a rapid decrease of crosswind Eulerian shear production P_E (the production due to the crosswind Eulerian shear and stress) and a relatively slow increase of along-wind P_E (the production due to the along-wind Eulerian shear and stress). For LT, the TKE production reduction is mainly caused by the rapid decrease of Stokes drift shear production P_S under misaligned wind and waves. During stage 2, the TKE production slowly increases and only slightly exceeds the TKE dissipation so that turbulence is approximately equilibrated with the wind and wave forcing. During stage 3, turbulence reaches its fully developed stage for all depths and is in equilibrium with the wind and wave forcing. At this stage, the adjustment of LT is slower than that of ST because of the slow relaxation of waves. Because waves are greatly misaligned during stages 1 and 2, TKE production by Eulerian shear significantly exceeds that due to Stokes drift shear. LT first weakens substantially after the wind turns and then recovers as waves align with the wind.

After the wind turns, the crosswind Eulerian velocity shear develops more slowly than the along-wind component in LT, while their developments are similar for ST. A Reynolds stress budget analysis shows that the contribution of turbulent stress from

Stokes drift is significant for the development of turbulent currents. With LT, the along-wind turbulent stress develops due to the increase of the Eulerian shear contribution, similar to ST. However, the decay of crosswind turbulent stress is also due to stress production from anti-Stokes Eulerian shear, which balances the Stokes production. The different along-wind stress dynamics and crosswind stress dynamics with LT lead to distinct velocity shear developments for the along-wind and crosswind directions.

LES results with different turning wind directions (AC/C cases) show obvious differences during stages 1 and 2. During stage 1, TKE is less reduced for the AC cases because of preconditioned Ekman shear that promotes TKE production for the AC cases and suppresses that for the C cases. The difference between C and AC is more pronounced for ST than LT due to smaller initial Eulerian shear in LT. During stage 2, the AC cases are characterized by a TKE overshoot with TKE levels substantially above those expected for constant winds, which is only partially due to inertial resonance. Another important contributor to the TKE overshoot involves temporarily reduced near-surface turbulence, which decreases the downward momentum transport and, in turn, results in substantial Eulerian velocity shear near the surface. Eventually, this shear becomes unstable to produce relatively high levels of TKE.

A comparison of RANS and LES model results reveal important strengths and limitations for applications of turbulence closure schemes to rapidly turning wind conditions. For ST cases, the RANS models based on the K-profile parameterization (KPP; Large et al. 1994) and second-moment closure (SMC; Kantha and Clayson 1994) turbulent models agree reasonably well with LES results. For C-ST, a simple RANS model that utilizes law-of-the-wall type scalings applied to the developing OSBL yields response time scales of TKE production that are consistent with LES results. For accurate RANS model with LT, however, it is critical for strongly transient and misaligned wind and wave conditions that stress production by Stokes drift and Eulerian shear is explicitly incorporated, such as is done for the SMC-LT model (Harcourt 2015). In summary, our study finds that transient wind and wave forcing significantly influences OSBL dynamics, playing a key role in the development of nonequilibrium turbulence.

REFERENCES

Belcher, S. E., and Coauthors, 2012: A global perspective on Langmuir turbulence in the ocean surface boundary layer. *Geophys. Res. Lett.*, **39**, L18605, https://doi.org/10.1029/2012GL052932.

Booij, N., L. Holthuijsen, and R. Ris, 1997: The "SWAN" wave model for shallow water. *Coastal Eng.*, **1996**, 668–676, https://doi.org/10.1061/9780784402429.053.

Craik, A. D., and S. Leibovich, 1976: A rational model for Langmuir circulations. *J. Fluid Mech.*, **73**, 401–426, https://doi.org/10.1017/S0022112076001420.

D'Asaro, E. A., 2001: Turbulent vertical kinetic energy in the ocean mixed layer. *J. Phys. Oceanogr.*, **31**, 3530–3537, https://doi.org/10.1175/1520-0485(2002)031<3530:TVKEIT>2.0.CO;2.

——, 2014: Turbulence in the upper-ocean mixed layer. *Annu. Rev. Mar. Sci.*, **6**, 101–115, https://doi.org/10.1146/annurev-marine-010213-135138.

——, J. Thomson, A. Shcherbina, R. Harcourt, M. Cronin, M. Hemer, and B. Fox-Kemper, 2014: Quantifying upper ocean turbulence driven by surface waves. *Geophys. Res. Lett.*, **41**, 102–107, https://doi.org/10.1002/2013GL058193.

Donelan, M. A., J. Hamilton, and W. Hui, 1985: Directional spectra of wind-generated ocean waves. *Philos. Trans. Roy. Soc. London*, **315A**, 509–562, https://doi.org/10.1098/rsta.1985.0054.

Ekman V. W., 1905: On the influence of the Earth's rotation on ocean-currents. *Ark. Mat. Astron. Fys.*, **2**, 1– 52.

Farmer, D., and M. Li, 1995: Patterns of bubble clouds organized by Langmuir circulation. *J. Phys. Oceanogr.*, **25**, 1426–1440, https://doi.org/10.1175/1520-0485(1995)025<1426:POBCOB>2.0.CO;2.

Gargett, A., J. Wells, A. Tejada-Martinez, and C. Grosch, 2004: Langmuir supercells: A mechanism for sediment resuspension and transport in shallow seas. *Science*, **306**, 1925–1928, https://doi.org/10.1126/science.1100849.

Harcourt, R. R., 2013: A second-moment closure model of Langmuir turbulence. *J. Phys. Oceanogr.*, **43**, 673–697, https://doi.org/10.1175/JPO-D-12-0105.1.

——, 2015: An improved second-moment closure model of Langmuir turbulence. *J. Phys. Oceanogr.*, **45**, 84–103, https://doi.org/10.1175/JPO-D-14-0046.1.

——, and E. A. D'Asaro, 2008: Large-eddy simulation of Langmuir turbulence in pure wind seas. *J. Phys. Oceanogr.*, **38**, 1542–1562, https://doi.org/10.1175/2007JPO3842.1.

Holthuijsen, L., A. Kuik, and E. Mosselman, 1987: The response of wave directions to changing wind directions. *J. Phys. Oceanogr.*, **17**, 845–853, https://doi.org/10.1175/1520-0485(1987)017<0845:TROWDT>2.0.CO;2.

Kantha, L. H., and C. A. Clayson, 1994: An improved mixed layer model for geophysical applications. *J. Geophys. Res.*, **99**, 25 235–25 266, https://doi.org/10.1029/94JC02257.

Kenyon, K. E., 1969: Stokes drift for random gravity waves. *J. Geophys. Res.*, **74**, 6991–6994, https://doi.org/10.1029/JC074i028p06991.

Kukulka, T., and R. R. Harcourt, 2017: Influence of Stokes drift decay scale on Langmuir turbulence. *J. Phys. Oceanogr.*, **47**, 1637–1656, https://doi.org/10.1175/JPO-D-16-0244.1.

——, A. J. Plueddemann, J. H. Trowbridge, and P. P. Sullivan, 2009: Significance of Langmuir circulation in upper ocean mixing: Comparison of observations and simulations. *Geophys. Res. Lett.*, **36**, L10603, https://doi.org/10.1029/2009GL037620.

——, ——, and P. P. Sullivan, 2013: Inhibited upper ocean restratification in nonequilibrium swell conditions. *Geophys. Res. Lett.*, **40**, 3672–3676, https://doi.org/10.1002/grl.50708.

Langmuir, I., 1938: Surface motion of water induced by wind. *Science*, **87**, 119–123, https://doi.org/10.1126/science.87.2250.119.

Large, W. G., J. C. McWilliams, and S. C. Doney, 1994: Oceanic vertical mixing: A review and a model with a nonlocal boundary layer parameterization. *Rev. Geophys.*, **32**, 363–403, https://doi.org/10.1029/94RG01872.

Lewis, D., and S. Belcher, 2004: Time-dependent, coupled, Ekman boundary layer solutions incorporating Stokes drift. *Dyn. Atmos. Oceans*, **37**, 313–351, https://doi.org/10.1016/j.dynatmoce.2003.11.001.

Li, M., C. Garrett, and E. Skyllingstad, 2005: A regime diagram for classifying turbulent large eddies in the upper ocean. *Deep-Sea Res. I*, **52**, 259–278, https://doi.org/10.1016/j.dsr.2004.09.004.

Li, Q., B. Fox-Kemper, Ø. Breivik, and A. Webb, 2017: Statistical models of global Langmuir mixing. *Ocean Modell.*, **113**, 95–114, https://doi.org/10.1016/j.ocemod.2017.03.016.

——, and Coauthors, 2019: Comparing ocean surface boundary vertical mixing schemes including Langmuir turbulence. *J. Adv. Model. Earth Syst.*, **11**, 3545–3592, https://doi.org/10.1029/2019MS001810.

Madsen, O. S., 1977: A realistic model of the wind-induced Ekman boundary layer. *J. Phys. Oceanogr.*, **7**, 248–255, https://doi.org/10.1175/1520-0485(1977)007<0248:ARMOTW>2.0.CO;2.

McWilliams, J. C., and P. P. Sullivan, 2000: Vertical mixing by Langmuir circulations. *Spill Sci. Technol. Bull.*, **6**, 225–237, https://doi.org/10.1016/S1353-2561(01)00041-X.

——, ——, and C.-H. Moeng, 1997: Langmuir turbulence in the ocean. *J. Fluid Mech.*, **334**, 1–30, https://doi.org/10.1017/S0022112096004375.

——, E. Huckle, J.-H. Liang, and P. P. Sullivan, 2012: The wavy Ekman layer: Langmuir circulations, breaking waves, and Reynolds stress. *J. Phys. Oceanogr.*, **42**, 1793–1816, https://doi.org/10.1175/JPO-D-12-07.1.

——, ——, J. Liang, and P. P. Sullivan, 2014: Langmuir turbulence in swell. *J. Phys. Oceanogr.*, **44**, 870–890, https://doi.org/10.1175/JPO-D-13-0122.1.

Moeng, C.-H., 1984: A large-eddy-simulation model for the study of planetary boundary-layer turbulence. *J. Atmos. Sci.*, **41**, 2052–2062, https://doi.org/10.1175/1520-0469(1984)041<2052:ALESMF>2.0.CO;2.

Pearson, B., 2018: Turbulence-induced anti-Stokes flow and the resulting limitations of large-eddy simulation. *J. Phys. Oceanogr.*, **48**, 117–122, https://doi.org/10.1175/JPO-D-17-0208.1.

Pollard, R. T., P. B. Rhines, and R. O. Thompson, 1973: The deepening of the wind-mixed layer. *Geophys. Fluid Dyn.*, **4**, 381–404, https://doi.org/10.1080/03091927208236105.

Polton, J. A., and S. E. Belcher, 2007: Langmuir turbulence and deeply penetrating jets in an unstratified mixed layer. *J. Geophys. Res.*, **112**, C09020, https://doi.org/10.1029/2007JC004205.

Price, J. F., and M. A. Sundermeyer, 1999: Stratified Ekman layers. *J. Geophys. Res.*, **104**, 20 467–20 494, https://doi.org/10.1029/1999JC900164.

——, R. A. Weller, and R. R. Schudlich, 1987: Wind-driven ocean currents and Ekman transport. *Science*, **238**, 1534–1538, https://doi.org/10.1126/science.238.4833.1534.

Rabe, T. J., T. Kukulka, I. Ginis, T. Hara, B. G. Reichl, E. A. D'Asaro, R. R. Harcourt, and P. P. Sullivan, 2015: Langmuir turbulence under Hurricane Gustav (2008). *J. Phys. Oceanogr.*, **45**, 657–677, https://doi.org/10.1175/JPO-D-14-0030.1.

Reichl, B. G., and Q. Li, 2019: A parameterization with a constrained potential energy conversion rate of vertical mixing due to Langmuir turbulence. *J. Phys. Oceanogr.*, **49**, 2935–2959, https://doi.org/10.1175/JPO-D-18-0258.1.

——, D. Wang, T. Hara, I. Ginis, and T. Kukulka, 2016: Langmuir turbulence parameterization in tropical cyclone conditions. *J. Phys. Oceanogr.*, **46**, 863–886, https://doi.org/10.1175/JPO-D-15-0106.1.

Skyllingstad, E. D., and D. W. Denbo, 1995: An ocean large-eddy simulation of Langmuir circulations and convection in the surface mixed layer. *J. Geophys. Res.*, **100**, 8501–8522, https://doi.org/10.1029/94JC03202.

——, W. Smyth, and G. Crawford, 2000: Resonant wind-driven mixing in the ocean boundary layer. *J. Phys. Oceanogr.*, **30**, 1866–1890, https://doi.org/10.1175/1520-0485(2000)030<1866:RWDMIT>2.0.CO;2.

Sullivan, P. P., and J. C. McWilliams, 2010: Dynamics of winds and currents coupled to surface waves. *Annu. Rev. Fluid Mech.*, **42**, 19–42, https://doi.org/10.1146/annurev-fluid-121108-145541.

——, L. Romero, J. C. McWilliams, and W. K. Melville, 2012: Transient evolution of Langmuir turbulence in ocean boundary layers driven by hurricane winds and waves. *J. Phys. Oceanogr.*, **42**, 1959–1980, https://doi.org/10.1175/JPO-D-12-025.1.

Thorpe, S., 2004: Langmuir circulation. *Annu. Rev. Fluid Mech.*, **36**, 55–79, https://doi.org/10.1146/annurev.fluid.36.052203.071431.

Umlauf, L., and H. Burchard, 2005: Second-order turbulence closure models for geophysical boundary layers: A review of recent work. *Cont. Shelf Res.*, **25**, 795–827, https://doi.org/10.1016/j.csr.2004.08.004.

Van Roekel, L., B. Fox-Kemper, P. Sullivan, P. Hamlington, and S. Haney, 2012: The form and orientation of Langmuir cells for misaligned winds and waves. *J. Geophys. Res.*, **117**, C05001, https://doi.org/10.1029/2011JC007516.

van Vledder, G. P., and L. Holthuijsen, 1993: The directional response of ocean waves to turning winds. *J. Phys. Oceanogr.*, **23**, 177–192, https://doi.org/10.1175/1520-0485(1993)023<0177:TDROOW>2.0.CO;2.

Wang, D., T. Kukulka, B. G. Reichl, T. Hara I. Ginis, and P. P. Sullivan, 2018: Interaction of Langmuir turbulence and inertial currents in the ocean surface boundary layer under tropical cyclones. *J. Phys. Oceanogr.*, **48**, 1921–1940, https://doi.org/10.1175/JPO-D-17-0258.1.

——, ——, ——, ——, and ——, 2019: Wind–wave misalignment effects on Langmuir turbulence in tropical cyclone conditions. *J. Phys. Oceanogr.*, **49**, 3109–3126, https://doi.org/10.1175/JPO-D-19-0093.1.

Young, I., and L. Verhagen, 1996: The growth of fetch limited waves in water of finite depth. Part I. Total energy and peak frequency. *Coast. Eng.*, **29**, 47–78, https://doi.org/10.1016/S0378-3839(96)00006-3.

——, S. Hasselmann, and K. Hasselmann, 1987: Computations of the response of a wave spectrum to a sudden change in wind direction. *J. Phys. Oceanogr.*, **17**, 1317–1338, https://doi.org/10.1175/1520-0485(1987)017<1317:COTROA>2.0.CO;2.